



Integration of multi-resource remotely sensed data and allometric models for forest aboveground biomass estimation in China

Huabing Huang^{a,*}, Caixia Liu^a, Xiaoyi Wang^a, Xiaolu Zhou^b, Peng Gong^c

^a State Key Laboratory of Remote Sensing Science, Institute of Remote Sensing and Digital Earth, Chinese Academy of Sciences, Beijing 100101, China

^b Ecological Modeling and Carbon Science, Department of Biology Science, University of Quebec at Montreal, Montreal, QC H3C 3P8, Canada

^c Ministry of Education Key Laboratory for Earth System Modeling, Department of Earth System Science, Tsinghua University, Beijing 100084, China

ARTICLE INFO

Keywords:

Forest aboveground biomass
Carbon storage
PALSAR imagery
ICESat/GLAS

ABSTRACT

Quantification of forest aboveground biomass density (AGB) is useful in forest carbon cycle studies, biodiversity protection and climate-change mitigation actions. However, a finer resolution and spatially continuous forest AGB map is inaccessible at national level in China. In this study, we developed forest type- and ecozone-specific allometric models based on 1607 field plots. The allometric models were applied to Geoscience Laser Altimeter System (GLAS) data to calculate AGB at the footprint level. We then mapped a 30 m resolution national forest AGB by relating the GLAS footprint AGB to various variables derived from Landsat images and Phased Array L-band Synthetic Aperture Radar (PALSAR) data. We estimated the average forest AGB to be 69.88 Mg/ha with a standard deviation of 35.38 Mg/ha and the total AGB carbon stock to be 5.44 PgC in China. Our AGB estimates corresponded reasonably well with AGB inventories from the top ten provinces in the forested area, and the coefficient of determination and root mean square error were 0.73 and 20.65 Mg/ha, respectively. We found that the main uncertainties for AGB estimation could be attributed to errors in allometric models and in height measurements by the GLAS. We also found that Landsat-derived variables outperform PALSAR-derived variables and that the textural features of PALSAR better support forest AGB estimates than backscattered intensity.

1. Introduction

Forest aboveground biomass density (AGB), measured in units of megagrams of mass per hectare, is often used to quantify forest contributions to the carbon cycle (Le Toan et al., 2011). The Group on Earth Observations – Biodiversity Observation Network identifies AGB as an essential biodiversity variable to measure ecosystem functions (Pettorelli et al., 2016). Although the AGB turnover time is slow, standard forest AGB patterns (e.g., benchmark mapping) remain poorly mapped due to a lack of field sample data and finer-resolution remotely sensed data unencumbered by clouds at the national scale (Gong, 2012).

China currently has the fifth largest total forested area in the world, and the forest volume has expanded continuously at an average rate of 2% each year (CMF, 2014). To mitigate climate change and to conserve forested areas, China plans to launch its national emissions trading system and focus on forest carbon stocks (Dong et al., 2016). Therefore, to develop a forest AGB benchmark map is critical for forest carbon stock estimations and for ongoing assessments.

Traditionally, forest AGB is calculated by allometric equations with

the tree heights and diameters measured in field plots. At the national scale, inventory-based approaches simply convert forest AGB from forest timber volumes (Zhou et al., 2016). However, different remote sensing technologies have recently been used as the primary tool for forest AGB estimation (Hall et al., 2011; Saatchi et al., 2011). Optical remote sensing can obtain reflected signals from canopy tops and be used to determine a limited correlation with forest AGB (Foody et al., 2003). Time-series or multi-seasonal optical images provide more usable information for AGB estimation, as they better capture forest structure dynamics than single date images (Boisvenue et al., 2016). Due to its capability of penetrating forest canopies and recording reflected signal from canopy tops and from ground, Light Detection and Ranging (LiDAR) is the most suitable technology to measure tree heights and to estimate forest AGB (Lefsky et al., 1999; Nelson et al., 2017). Biomass-height relationships have been developed at the plot level based on field AGB samples and different variables from LiDAR data (Cao et al., 2016). While achieving significant progress toward direct measurement, existing LiDARs in space (e.g., ICESat/GLAS) generate only samples and transects and cannot produce wall-to-wall coverage of a large area (Sun et al., 2011). Unlike passive optical

* Corresponding author.

E-mail address: huanghb@radi.ac.cn (H. Huang).

<https://doi.org/10.1016/j.rse.2018.11.017>

Received 18 August 2017; Received in revised form 3 November 2018; Accepted 10 November 2018

Available online 23 November 2018

0034-4257/ © 2018 Elsevier Inc. All rights reserved.

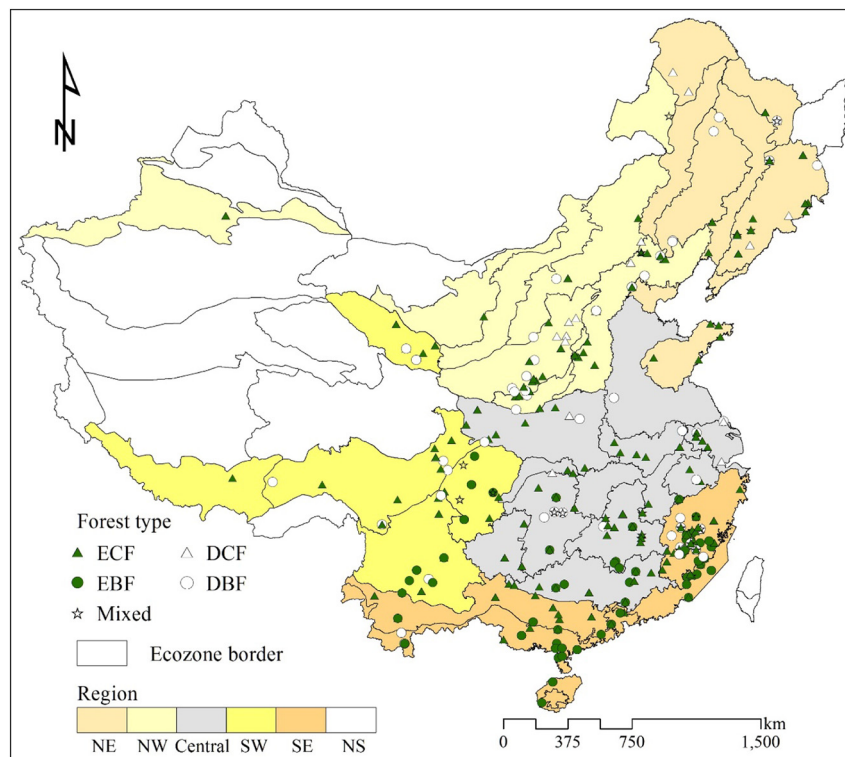


Fig. 1. Spatial distribution of field plots of five forest types in different ecozones. NE denotes northeastern China, NW denotes northwestern China, SW denotes southwestern China and SE denotes southeastern China. NS denotes that there are no field plots in a given region.

images or LiDAR, synthetic aperture radar (SAR) is not affected by cloud cover or lighting conditions and shows great potential for forest AGB estimation (Thiel and Schullius, 2016). SAR backscattering depends on its wavelength and geometrical and dielectric features of various scatterers (leaves, branches and stems) (Dobson et al., 1992; Ferrazzoli and Guerriero, 1995; Rignot, 1996; Santi et al., 2017; Ulaby et al., 1990). L-band SAR has better canopy penetration capacity than X-band SAR and optical images so they produce less saturation problem (Baghdadi et al., 2015; Castel et al., 2000; Villard et al., 2016). Texture information generated from SAR data can identify different aspects of forest stand structure, such as tree height, crown diameter, and density (Sarker et al., 2013). However, texture from L-band SAR images and its role in forest AGB estimation has not yet been fully documented and rarely seen in practice, especially when combined with other remotely sensed data for AGB estimation in large areas (Rodríguez-Veiga et al., 2016; Thapa et al., 2015).

Although the abovementioned techniques have been tested in regards to biomass estimations from space through various studies, in situ forest AGB samples are crucial for relating remotely sensed data to the estimated AGB (Duncanson et al., 2015). Most studies have used empirical or semi-empirical models to invert biomass through multiple variable regressions between in situ AGB samples and variables derived from different remotely sensed data (Chi et al., 2015). However, basic ecological information, such as height-based or height and diameter combined allometric relations and, in particular, forest type- and ecozone-specific allometric models, have rarely been used to estimate forest AGB at the national scale (Rodríguez-Veiga et al., 2016).

In this study we attempt to develop forest type and ecozone-specific AGB-H allometric models based on field forest samples, and to produce a finer resolution forest AGB map using ICESat/GLAS, Landsat, L-band PALSAR, and topographic data. We then optimize the potential of each dataset to exploit the specific strengths of multi-source remotely sensed data to circumvent the saturation problem in a single sensor for forest AGB estimation over large areas. The objectives of this study are as follows:

- (1) To develop a new and finer resolution (30 m) forest AGB map in China and to analyze its spatial patterns and related uncertainties,
- (2) To explore contributions of various variables extracted from multi-source remotely sensed data to AGB estimation, and
- (3) To assess the accuracy of the estimated forest AGB with that derived from the Chinese National Forest Inventory in thirty-one provinces.

2. Data and methods

2.1. Construction of the allometric model from field plots

Field plots were collected from a comprehensive database of Chinese forest biomass for the past three decades. The dataset includes biomass data for stems and other aboveground components such as branches, leaves and bark. It also includes geographic locations, forest types, dominant species, heights, climates, soil fertility levels, stands, sample sizes and biomass measurement methods. The dataset includes 1607 field plots that cover the entire forested area of China, and 650 of the plots were collected after 2000 (Luo et al., 2013). We verified the dataset and filtered 559 incomplete samples that did not include forest types, dominant species, heights, stem biomass and AGB. We then divided the remaining 1048 samples by forest type and ecozone to construct allometric models (Fu et al., 2004). Five forest types were considered (evergreen conifer forest (ECF), deciduous conifer forest (DCF), evergreen broadleaf forest (EBF), deciduous broadleaf forest (DBF), and mixed forest) based on a 30 m forest type map, which was produced by 30 m Landsat Thematic Mapper (TM) data and 250 m time series Enhanced Vegetation Index (EVI) from Moderate Resolution Imaging Spectrometer (MODIS) (Li et al., 2014). To ensure enough samples for constructing an allometric model and can pass the significance test at $p < 0.05$ level for each forest type, we incorporated ecozones into the five regions according to geographic and climatic conditions (Fig. 1). For individual forest types of different regions, a two-step allometric model was developed to convert heights into AGB (Cheng et al., 2007; Liu et al., 2017). As height accounted for 87.2% of the stem biomass

variance, and as stem biomass explained nearly all the variation (97.2%) in AGB (Luo et al., 2013), the stem biomass was used as an intermediate variable to reduce the AGB calculation bias directly from the height (Zhou et al., 2016).

$$\begin{aligned} AGB_{stem} &= aH^b \\ AGB_{above} &= mAGB_{stem}^n \end{aligned} \quad (1)$$

where AGB_{above} is the aboveground biomass density, measured in units of megagrams (Mg) of mass per hectare (ha), AGB_{stem} is the stem biomass density, and H is the mean height of dominant trees from the emergent layer and the canopy layer in a field plot. a , b , m and n are the power function parameters.

2.2. Forest canopy height extraction from ICESat/GLAS data

The transmitted and received waveform data (GLA01) and waveform parameterization data (GLA05) from the Geoscience Laser Altimeter System (GLAS) on board the Ice, Cloud, and Land Elevation Satellite (ICESat) were used to extract forest canopy height. These data were from release 33 and obtained in 2006 (Zwally et al., 2011). First, the footprints from non-forested areas were filtered using a forest type map (Li et al., 2014). Then, a Gaussian decomposition algorithm was used to assess the number of peaks in each footprint (Gong et al., 2011). The footprint was discarded, if the decomposed Gaussian waveforms had only one peak, because waveforms returned from the forest included at least two peaks, i.e. the ground and the canopy layers. The forest canopy height at the GLAS footprint level was determined using Eq. (2):

$$FCH = gpCntRng(1) - SigBeg \quad (2)$$

where FCH is the forest canopy height, $gpCntRng(1)$ is the center position of the ground peak, which is the stronger peak of the lowest two from the decomposed Gaussian peaks, and $SigBeg$ denotes the start of the earliest return peak corresponding to a forest canopy. Finally, a topographic correction method was used to determine the waveform-broadening effects on height extraction in rugged areas due to topography (Wang et al., 2014).

$$FCH_{slope} = gpCntRng(1) - SigBeg - 3 \times (\sigma_{gp} - \sigma_{transmit}) \quad (3)$$

In Eq. (3), FCH_{slope} denotes the forest height of a rugged area; in this study, a ‘rugged area’ is defined as a region with a slope $> 5^\circ$. Footprints with slopes larger than 25° were filtered for further processing, as determined by previous studies (Simard et al., 2011; Wang et al., 2014). σ_{gp} is the standard deviation of the Gaussian function from the ground peak and it represents the width of a ground peak, and $\sigma_{transmit}$ is defined as the standard deviation of the Gaussian function from a transmitted waveform.

The final GLAS dataset includes 92,490 forest canopy height measurements for all of China. These heights were converted to stem biomass density levels (AGB_{stem}) and then to AGB density levels (AGB_{above}) using the allometric models (Eq. (1)) developed from field plots.

2.3. Variables derived from the Landsat 5 thematic mapper (TM) composites

We collected 6540 Landsat 5 TM standard surface reflectance images for 2006 from the Google Earth Engine (GEE). These images were processed with the LEAPS method (<http://ledaps.nascom.nasa.gov/>, accessed 19.03.17) and a cloud mask algorithm (Zhu et al., 2015). We masked pixels of shadows and clouds in the cloud mask band by assigning a value of 2 to shadows and a value of 4 to clouds. We then calculated the normalized difference vegetation index (NDVI).

Variables were generated according to a previous study on tree height mapping in Sub-Saharan Africa (Hansen et al., 2016). First, the red, near-infrared (NIR) and shortwave infrared bands (SWIR) were

sorted from minimum to maximum reflectance values. Then, the means for inter-percentile ranges of 10 to 90 (P1090), 10 to 25 (P1025), 25 to 75 (P2575), and 75 to 90 (P7590) were calculated for all bands and NDVI per pixel and for 3×3 moving window kernels to reduce outliers.

2.4. Texture features extraction from the PALSAR mosaic dataset

The PALSAR mosaic dataset was aggregated from Phased Array L-band Synthetic Aperture Radar (PALSAR) data from 2007 to 2010 (Shimada et al., 2014). Original SAR data was obtained using the fine beam dual polarization (FBD) mode, which provides HH and HV data. The geometric distortion and topographic effects on PALSAR images were reduced via ortho-rectification, and the geometric accuracy was estimated at 12 m (Qin et al., 2015).

In order to have a simultaneous dataset with Landsat and GLAS, we used PALSAR data from 2007. To achieve consistency among the datasets, we resampled HH and HV data to 30 m through nearest neighbor interpolation. We also calculated texture features from previous studies using the Gray Level Co-occurrence Matrix (Conners et al., 1984; Haralick et al., 1973). GEE functions were used to compute all texture features for each pixel with a 3×3 window.

2.5. Topographic features derived from Shuttle Radar Topography Mission (SRTM) data

SRTM digital elevation model (DEM) data were released in 2015 with a resolution of 30 m. This dataset has been through a void-filling process (Reuter et al., 2007) whereby slopes (Moore et al., 1991) were extracted as an input variable for subsequent modeling. The SRTM DEM was also used to calculate the pixel slopes covered by all ICESat/GLAS footprints. Specifically, the pixel slope was calculated as the mean of the slopes of the grid cell for which the GLAS measurement was collected.

2.6. Spatially continuous AGB estimation

We used the Random Forest regression tree (RF) model to extrapolate 92,490 AGB_{GLAS} into spatially continuous AGB values (Fig. 2). The RF model can process a large number of input predictors that are not independent or non-linearly separable, so it is especially useful for monitoring complex ecological systems (i.e. forest height, biomass estimation and forest classification) using variables from different remote sensing measurements (Belgiu and Drăguț, 2016; Huang et al., 2017; Liu et al., 2015; Saatchi et al., 2011).

We trained the RF model by relating AGB_{GLAS} with variables derived from Landsat TM, PALSAR, SRTM, and forest type data. The RF trees were created by drawing a subset of training samples (AGB_{GLAS}) through the bootstrap approach. 90% of AGB_{GLAS} were used to train the model, and the remaining 10% were used to validate the model. The number of trees ($N_{tree} = 300$), and of variables split in each node ($M_{try} = 19$) were determined iteratively with a pre-test. The out-of-bag (OOB) error is a reliable measure for RF model accuracy and variables importance (Belgiu and Drăguț, 2016). Specifically, the RF model computes the average increase in the mean square error (%IncMSE) by permuting OOB data for a variable while keeping all other variables constant (Pflugmacher et al., 2014). We chose 56 higher ranking variables (Table S1) from a total of 83 variables based on their OOB errors with a pre-test. For those variables, we also reported their contribution to final forest AGB estimation in Section 3.4. After an ensemble decision tree was incorporated into the training procedure, the rules of each decision tree along with two optimal parameters were used to predict the spatially continuous AGB. Optimal parameter determination and variables importance ranking were performed using the random forest package in MATLAB, and the RF model was executed using the GEE random forest regression function.

Non-forested areas were masked with a forest type map (Li et al.,

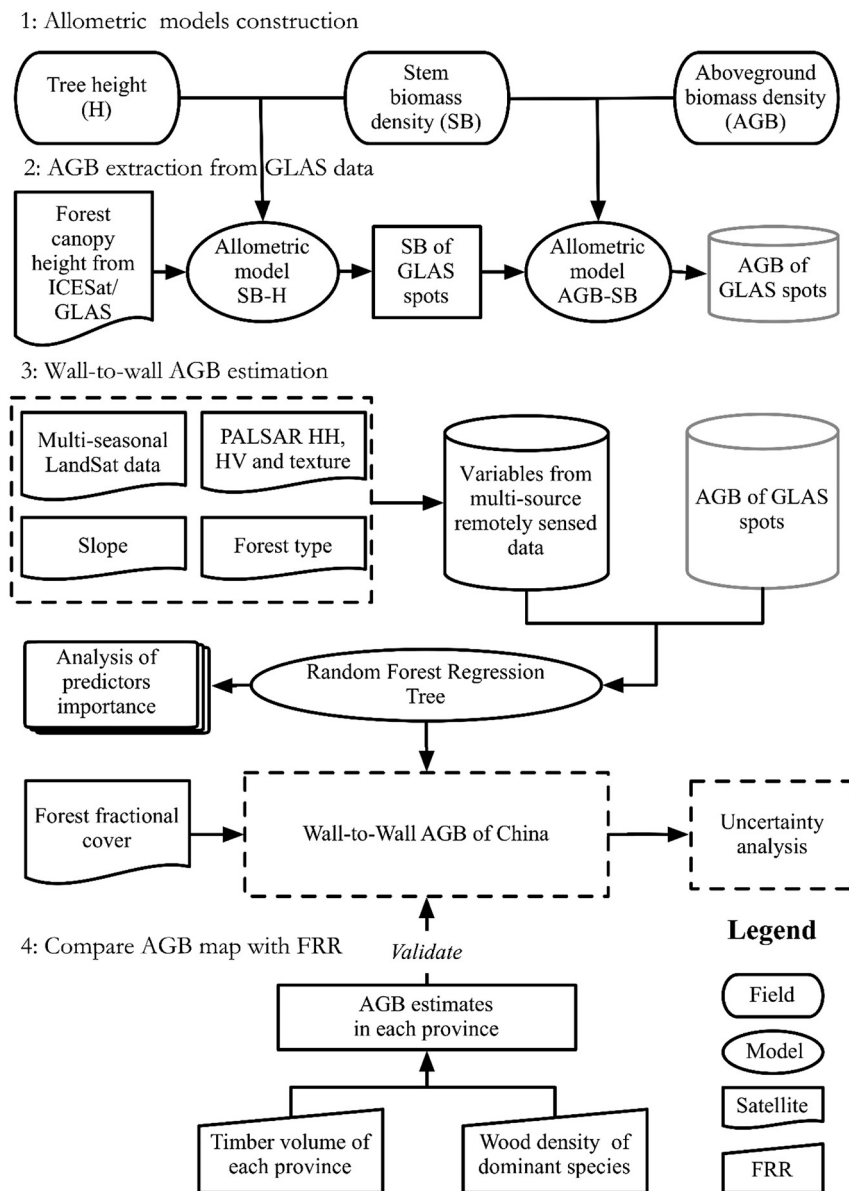


Fig. 2. Overall workflow of the forest AGB estimation. FRR: Chinese forest resource reports.

2014). In order to exclude recently deforested and degraded areas, we assigned these AGB values to each 30 m pixel by correcting for satellite-derived canopy fraction cover, for example, a pixel that appeared half-forested was assigned half of the AGB values. (Asner et al., 2011; Sexton et al., 2013).

2.7. Uncertainty analysis

We measured the total uncertainty of the AGB estimation by quantifying errors associated with tree measurements in the field, through forest canopy height extraction from GLAS, through AGB-H model construction, by determining GLAS footprints and their distributions, and by measuring the uncertainty of the spatially continuous AGB prediction. All parts were reported in terms of the relative error, which is the root mean square error (RMSE) or the standard deviation divided by the estimated or measured mean (Chen et al., 2015). The error was calculated using the following equation:

$$\epsilon_{AGB} = (\epsilon_{height}^2 + \epsilon_{allometry}^2 + \epsilon_{GLAS_height}^2 + \epsilon_{sampling}^2 + \epsilon_{prediction}^2)^{1/2} \quad (4)$$

The tree height measurement error (ϵ_{height}) averaged on the plot

scale was assumed to be valued at 10% according to previous studies (Chave et al., 2004; Chen et al., 2016), which is greater than the tolerance level (5%) used for tree height measurements in the Chinese National Forest Inventory (Zeng et al., 2015). The error of the AGB-H allometric equations ($\epsilon_{allometry}$) was estimated by calculating the RMSE of specific forest types of different regions. The error originating from GLAS forest canopy height extraction (ϵ_{GLAS_height}) was obtained from a previous national forest height study; the RMSE was estimated as 4.31 m when validated with the mean height of dominant and co-dominant trees in forest plots (Lefsky et al., 2007), denoting a relative error of 26.9% for an average height of 16.01 m (Huang et al., submitted). The quantity and distribution of GLAS footprints was used to denote the sampling error ($\epsilon_{sampling}$) when extrapolating AGB for areas without corresponding GLAS footprints. To qualify this uncertainty, we randomly collected ten subsets with 55–100% GLAS footprints (at an interval of 5%). Ten AGB estimates were then modeled, and the deviation for each pixel was calculated to measure the sampling error associated with the number and distribution of GLAS footprints. The prediction error ($\epsilon_{prediction}$) was calculated through cross validation while running the RF model.

2.8. Forest AGB validation data collection

Because GLAS data and other remotely sensed images were acquired around 2006, it is hard to find enough field plots in 2006 to validate our AGB. In this situation, we collected an independent field AGB dataset from a previous study, which provided 189 field sampling sites (Zhu et al., 2017). These field sample points were measured between 2011 and 2016, and covered the main forest biomes in China. In order to minimize the effects of the time inconsistencies between our estimated AGB and those from the 189 field sample locations, we used Google's time-series image slider function to visually inspect all available high-resolution images to check these samples and chose the correct samples according to the following rules:

- The sample sites were in a uniform forest (at least 5×5 pixels) and their tree cover were $> 80\%$ to reduce the error in locating field plots.
- The greenest NDVI (2000–2016) time-series of the samples was stable and no forest disturbance happened during 2000–2016.
- The field measured AGB were corrected by satellite-derived canopy fraction cover to reduce the impact of tree cover change during 2006 to 2011 or even later (2016) (Sexton et al., 2013).

Finally, 61 field sample locations meeting the above conditions and were used to validate AGB map at pixel level.

We also collected forest AGB data from the Chinese forest resource reports (FRR) issued by the State Forest Administration. The FRR reported forest areas and timber volumes at the provincial level. We retrieved wood densities and timber volumes from the FRR for 2004–2008 and weighted them by forest areas for thirty-one provinces in mainland China (Zanne et al., 2009). From weighted timber volumes, wood densities, and a biomass expansion factor, we finally converted the timber volumes to forest AGB values for all provinces (Fang et al., 1998), and used these thirty-one AGBs as “true” observations to validate our AGB estimators at the provincial level.

3. Results

3.1. Allometric models of forest types and ecozones

Fig. 3 shows the distribution of tree heights, stem biomass density (SB) levels and AGB collected from 1048 field inventory samples. The mean height, SB and AGB were 10.70 m, 67.52 Mg/ha and 89.51 Mg/ha, respectively. The plot with the greatest height and AGB values was found to be an evergreen conifer forest in Tibet, and the measured tree heights and AGB were up to 65.1 m and 1433.21 Mg/ha. Mixed forest field inventory samples from the NE and NW; DCF samples from central, SE and SW; and DBF samples from central, SE and SW were incorporated according to forest type, because there were too few samples to build an allometric model that could pass the significance test of

$p < 0.05$. Table 1 lists the parameters of all allometric models for different forest types and regions. A scatter plot of one of the allometric models is shown in Fig. 4 and all of them are shown in Fig. S1. Overall, height accounted for 78% of the variation in stem biomass on average, and it varied from 67% for EBF in the central and SE regions to 93% for ECF in the SW region. Stem biomass consistently accounted for almost all the variation in AGB (98% on average). AGB-SB models presented smaller RMSE and relative error (8.22 Mg/ha and 9%) than SB-H models (23.91 Mg/ha and 35%). For SB-H models, DBF in the NW and ECF in the SW presented higher RMSE values (42.86 Mg/ha and 44.09 Mg/ha, respectively) than other forest types.

3.2. Model performance and variables contribution

Estimated AGB from the RF model versus that of GLAS-training data are plotted in Fig. 5 and the variation in training data density is also illustrated. The estimated AGB correlated well with the GLAS derived AGB ($R^2 = 0.72$, RMSE = 35.98 Mg/ha), while the RF model over-estimated low biomass and underestimated high biomass.

The predictor variables were ranked on the basis of the %IncMSE. Fig. 6 shows their relative contribution to AGB estimation among five forest types. The variables from Landsat data were more important than variables from other data. Specifically, eight variables derived from the red band (B3-related) were the highest-ranking variables for estimating forest AGB (15.15%). The NDVI-related variables contributed the second highest (14.50%), and texture features from HH band were ranked third (11.01%). Moreover, HV was ranked higher than HH for the AGB estimation and especially for DCF. Comparatively, textures from HH were ranked higher than that from HV.

The AGB was classified into seven groups at an interval of 50 Mg/ha to explore the contribution of variables along the AGB distribution (Fig. 7). Landsat B3-B7 bands showed the maximum contribution (53.64%) for the AGB class up to 100–150 Mg/ha, but after this point ranks decreased slightly. Above 150 Mg/ha, variables derived from the PALSAR data (HH and HV and their textures) became more important and then their contributions reached the maximum (35.18%) when the AGB class was 200–250 Mg/ha. The decline in the ranking of Landsat data after 150 Mg/ha and of PALSAR data after 250 Mg/ha denoted the saturation limit of Landsat data and the ability of L-band PALSAR for estimating high biomass. The forest type and slope together (25.91%) eventually became the highest-ranking variables at the highest AGB ranges (> 300 Mg/ha), which can be explained by the specific forest AGB distribution for China across the topographic gradient; for example, the highest AGB values in Tibet, Sichuan, and Taiwan are commonly accompanied by complex terrain.

3.3. Spatial pattern of AGB and their uncertainties

The 30 m resolution forest AGB map of China showed a broad range of forest AGB levels ranging from < 10 Mg/ha for dry desert grassland

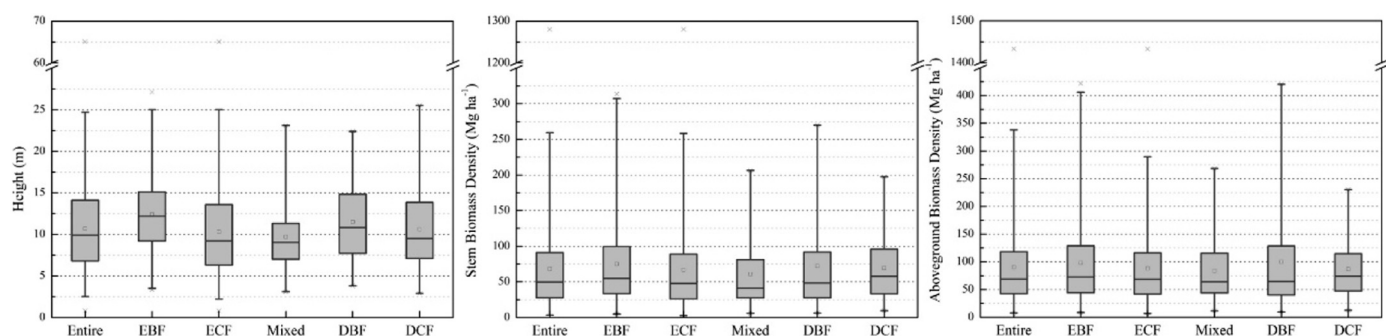


Fig. 3. Distribution of height, SB and AGB values derived from field plots of the forest types. The boxes show data within the range of the median \pm SD, the square denotes the mean, the dash denotes a whisker of 5–95%, and the cross denotes minimum and maximum values.

Table 1

Parameters that fit the SB-H and AGB-SB allometric models by forest types in different regions. a, b and m, n are the power function parameters for SB-H and AGB-SB allometric models, respectively. RMSE, R^2 , RE and S are the standard error, coefficient of determination, relative error and number of field plots, respectively.

| Forest type/region | SB-H | | | | | AGB-SB | | | | | |
|--------------------|----------|------|-------|-------|--------|--------|------|-------|-------|--------|-----|
| | α | b | RMSE | R^2 | RE (%) | m | n | RMSE | R^2 | RE (%) | S |
| ECF/NE | 1.77 | 1.48 | 19.22 | 0.80 | 37 | 3.1 | 0.81 | 6.58 | 0.98 | 9 | 92 |
| DCF | 5.46 | 1.1 | 18.9 | 0.77 | 28 | 1.54 | 0.94 | 5.24 | 0.99 | 6 | 43 |
| DBF | 0.43 | 1.96 | 17.16 | 0.76 | 27 | 1.7 | 0.94 | 8.64 | 0.96 | 10 | 18 |
| Mixed | 0.68 | 1.79 | 24.4 | 0.82 | 41 | 1.71 | 0.95 | 8.34 | 0.99 | 10 | 10 |
| ECF/NW | 2.64 | 1.36 | 15.71 | 0.80 | 35 | 2.53 | 0.86 | 6.42 | 0.98 | 10 | 89 |
| DCF | 2.05 | 1.47 | 24.03 | 0.77 | 36 | 2.82 | 0.83 | 10.83 | 0.97 | 12 | 34 |
| DBF | 0.7 | 1.92 | 42.86 | 0.73 | 48 | 1.68 | 0.97 | 11.37 | 0.99 | 9 | 34 |
| Mixed | 0.68 | 1.79 | 24.4 | 0.82 | 41 | 1.71 | 0.95 | 8.34 | 0.99 | 10 | 10 |
| ECF/central | 0.69 | 1.88 | 26.11 | 0.78 | 42 | 2.2 | 0.88 | 8.1 | 0.98 | 10 | 197 |
| EBF | 0.55 | 1.87 | 18.04 | 0.67 | 25 | 1.97 | 0.9 | 7.37 | 0.96 | 8 | 14 |
| DCF | 2.17 | 1.36 | 24.62 | 0.80 | 30 | 2.09 | 0.89 | 4.81 | 0.99 | 5 | 11 |
| DBF | 0.19 | 2.34 | 26.66 | 0.76 | 47 | 1.86 | 0.92 | 7.93 | 0.99 | 11 | 35 |
| Mixed | 2.92 | 1.32 | 18.83 | 0.75 | 29 | 3.74 | 0.76 | 10.34 | 0.94 | 12 | 16 |
| ECF/SE | 1.68 | 1.55 | 26.94 | 0.81 | 36 | 2.38 | 0.86 | 6.12 | 0.99 | 7 | 200 |
| EBF | 1.28 | 1.62 | 36.2 | 0.67 | 45 | 2.2 | 0.88 | 8.1 | 0.97 | 8 | 105 |
| DCF | 2.17 | 1.36 | 24.62 | 0.80 | 30 | 2.09 | 0.89 | 4.81 | 0.99 | 5 | 11 |
| DBF | 0.19 | 2.34 | 26.66 | 0.76 | 47 | 1.86 | 0.92 | 7.93 | 0.99 | 11 | 35 |
| Mixed | 1.12 | 1.74 | 22.21 | 0.82 | 36 | 2.92 | 0.82 | 7.81 | 0.98 | 9 | 47 |
| ECF/SW | 0.44 | 1.9 | 44.09 | 0.93 | 41 | 2.25 | 0.9 | 16.98 | 0.99 | 12 | 56 |
| EBF | 0.37 | 1.85 | 13.14 | 0.72 | 30 | 1.17 | 1.01 | 6.18 | 0.95 | 12 | 38 |
| DCF | 2.17 | 1.36 | 24.62 | 0.80 | 30 | 2.09 | 0.89 | 4.81 | 0.99 | 5 | 11 |
| DBF | 0.19 | 2.34 | 26.66 | 0.76 | 47 | 1.86 | 0.92 | 7.93 | 0.99 | 11 | 35 |
| Mixed | 2.11 | 1.43 | 11.28 | 0.82 | 18 | 3.03 | 0.81 | 6.85 | 0.95 | 8 | 9 |
| Average | | | 23.91 | 0.78 | 35 | | | 8.22 | 0.98 | 9 | |

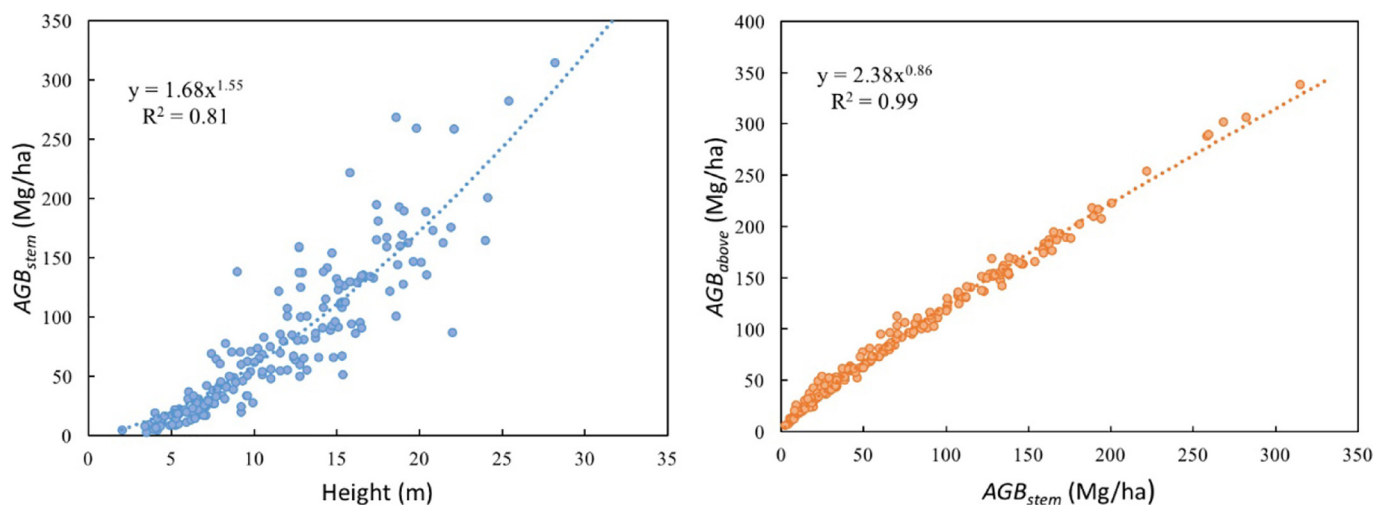


Fig. 4. Scatter plots for the SB-H (left) and AGB-SB (right) regression equations for evergreen conifer forest in southeastern China (ECF/SE listed in Table 1). The blue dots and line denote regression curves for the SB-H equation, the orange dots and line denote regression curves for the AGB-SB equation. (For interpretation of the references to color in this figure legend, the reader is referred to the web version of this article.)

and forest mosaic systems of the northeastern Altai and western Junggar mountains to > 500 Mg/ha for the tropical and monsoon forests of southeastern Tibet (Fig. 8). The average forest AGB in China was 69.88 Mg/ha with a standard deviation of 35.38 Mg/ha. The uncertainty in AGB varied from 35.75% to 85.31%, and the average uncertainty was 49.14%. Overall, the forest AGB for southern China was higher than that for northern China. A total AGB carbon stock for China of 5.44 PgC was inferred by summing the total AGB for all forest pixels (1.56×10^5 ha) from FRR for 2005 and using an AGB-to-carbon ratio of 0.5 (Piao et al., 2005).

3.4. Accuracy assessment of AGB map

The estimated AGB correlated well with 61 field measured AGB at pixel level and the coefficient of determination (R^2) and RMSE were

0.64 and 15.62 Mg/ha, respectively (Fig. 9). The uncertainty in validation of our AGB with the above field sample sites must be acknowledged, our AGB map cannot overlap with 61 field sample sites in time, more and simultaneous sample locations may improve the validation accuracy.

The estimated AGB also showed reasonable correspondence to that from the FRR in thirty-one provinces ($R^2 = 0.54$, RMSE = 19.26 Mg/ha; Fig. 10). Values for twenty-five provinces were overestimated, and those for six provinces were underestimated relative to FRR results. Moreover, Beijing and Zhejiang provinces presented obvious differences in absolute (> 50 Mg/ha) or percentage errors (> 150%). However, the estimated AGB of the top ten provinces in the forested area, which include 67% forested areas in China, presented a better correlation with the AGB of the FRR. The R^2 and RMSE were 0.73 and 20.65 Mg/ha, respectively (Fig. 10).

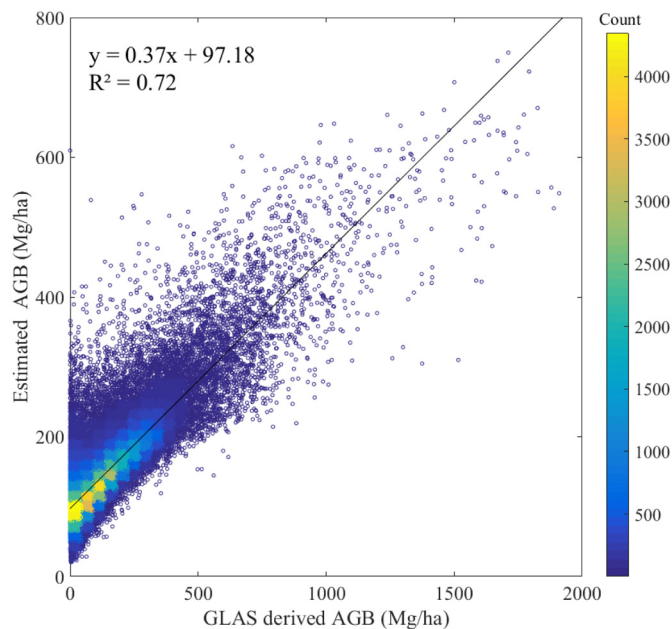


Fig. 5. The estimated AGB versus the GLAS-derived AGB and the density of GLAS training data.

4. Discussion

Forest biomass and carbon derived from previous studies at the national scale were converted into forest AGB to compare with our estimates using an AGB-to-carbon conversion factor of 0.5 and a forest biomass (aboveground and belowground) to AGB conversion factor of 0.81 (Luo et al., 2013). Our average AGB value was similar to three national forest AGB estimates made based on the forest timber volume of national forest inventories (Table 2) (Du et al., 2014; Piao et al., 2005; Yu et al., 2010). This level of consistency shows that the new method of integrating multi-source remotely sensed data and allometric models is feasible for monitoring national forest AGB. Yu et al. reported that Chinese forest carbon density levels have not changed significantly

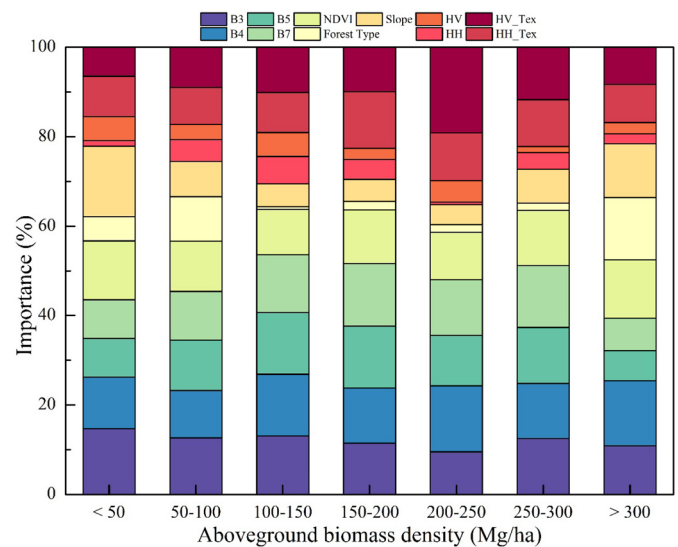


Fig. 7. Levels of variable importance along AGB ranges. The variables are indicated by different colors. Detailed definition of all variables was list in Table S1.

from the 1980s (Yu et al., 2010). To some extent, our results support their conclusion, because AGB estimates from the first four studies in Table 2 are concentrated within a narrow range (61.8–73.4 Mg/ha). Our AGB estimates are also lower than two forest AGB estimates primarily derived from MODIS data and field plots (Su et al., 2016; Yin et al., 2015). This may be attributable to the use of different types and resolutions of remotely sensed data and to different AGB estimation methods. We believe that the 30 m finer resolution AGB map is more consistent with the field plot data. Therefore, the scale mis-match is reduced when compared with those studies using low resolution remotely sensed data. Moreover, we constructed the allometric models through limited field plots and transmitted the ecological information to GLAS data rather than using empirical or semi-empirical biomass prediction models. In this way, we enrich the AGB samples into the number of GLAS spots. More training samples may be helpful to

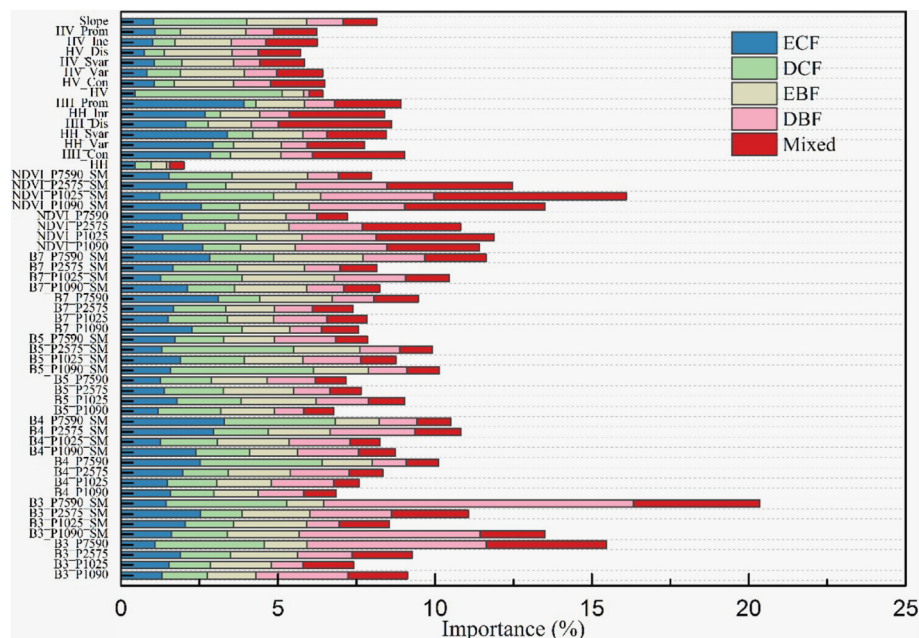


Fig. 6. The importance ranking of all variables for forest AGB modeling in different forest types. ECF: evergreen conifer forest, DCF: deciduous conifer forest, EBF: evergreen broadleaf forest, DBF: deciduous broadleaf forest, Mixed: mixed forest. Detailed definition of 56 variables is listed in Table S1.

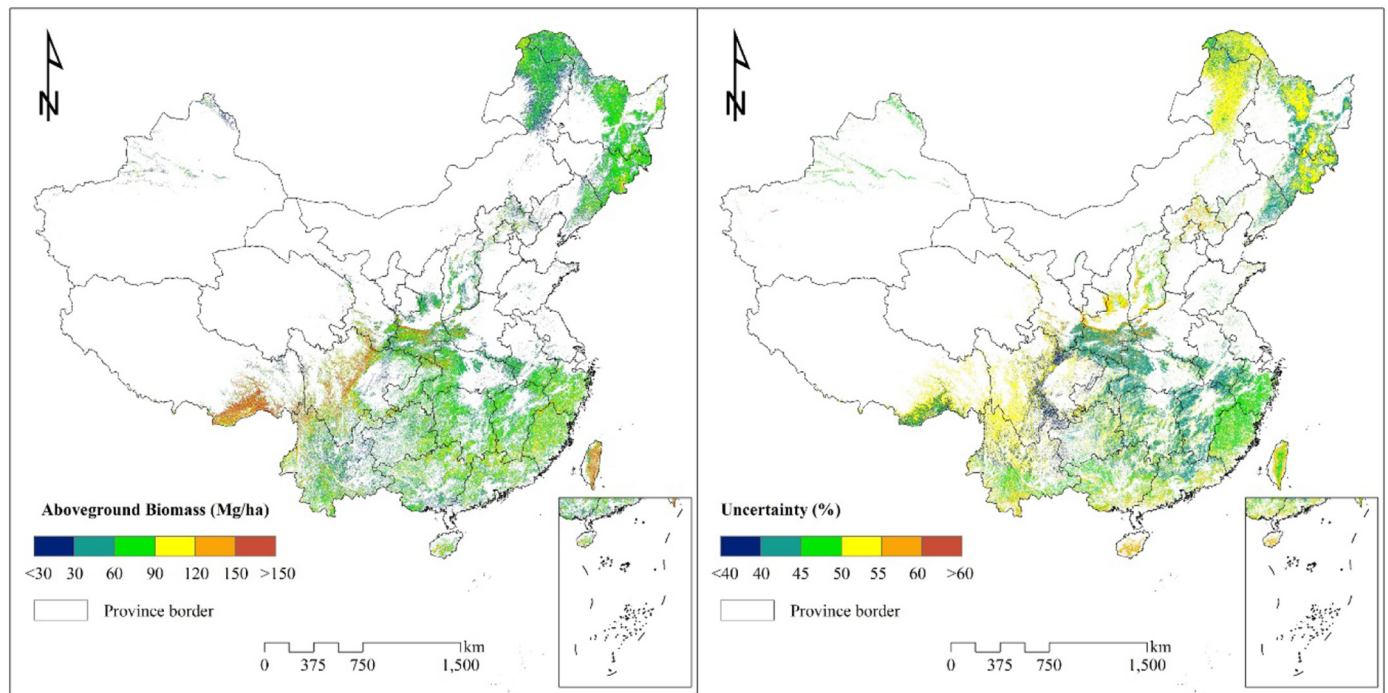


Fig. 8. Spatial distribution of the forest AGB for China (left) and the associated uncertainty level (right).

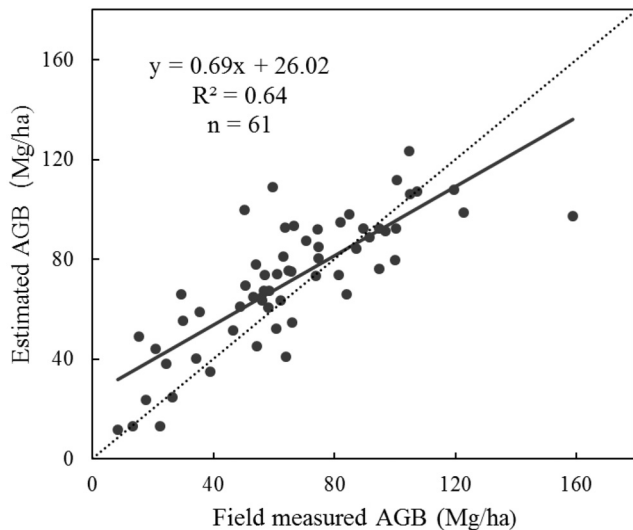


Fig. 9. Relationships between field measured AGB and the estimated AGB. The dashed line represents the 1:1 line.

develop a robust RF regression tree for modeling spatially continuous AGB values.

The greatest levels of uncertainty were derived from the allometric models (average 35% for the SB-H models and 9% for the SB-AGB models), and height measured via GLAS also contributed a large proportion to the total error (26.9%, as shown in Section 2.7). The field tree height measurement (10%), uncertainty level of number and distribution of GLAS footprint (6.58%), and model prediction (8.97%) introduced the remainder of the uncertainty. While we collected data on 1607 field plots, this dataset is too small to construct a flawless SB-H allometric model, especially given the diversity of forest types and ecozones in China. Although heights were the most relevant to stem biomass and explained 78% of the variation in stem biomass in this study, other forest structural parameters such as diameters at breast height (DBH) and crown widths, which can be measured from space,

should be integrated to reduce errors in SB-H models (Gong et al., 2002; Huang et al., 2009; Jucker et al., 2017).

Our variable importance ranking showed that texture features of PALSAR data contribute more than the backscattered intensity to AGB estimations. This finding indicates that textural features are more sensitive to forest AGB by measuring the canopy occurrence and unevenness among different forest types (Sarker et al., 2013; Thapa et al., 2015). Our results also showed that the Landsat-derived variables outperformed the PALSAR-derived variables for forest AGB estimation. This conclusion contrasts with that of a recent forest AGB study in Mexico, which found that PALSAR data are the most important predictors. The result also complements that of another study, which showed that the optical layer is superior (Cartus et al., 2014; Rodríguez-Veiga et al., 2016). Although there are currently no consistent results on the importance of optical images and SAR data, we believe that by integrating different data sources, the saturation of forest AGB estimations can be reduced, especially when multi-seasonal Landsat data are used. Such data can reveal spatial structure more effectively than a single date image.

5. Conclusions

We developed a finer resolution forest AGB estimation method and explored uncertainty sources. The average forest AGB of China is 69.87 Mg/ha with a standard deviation of 35.38 Mg/ha. Furthermore, China's total AGB carbon stock is 5.44 PgC. Our AGB estimates corresponded reasonably well with AGB inventories from the top ten provinces in the forested area, and the coefficient of determination and root mean square error were 0.73 and 20.65 Mg/ha, respectively. A comprehensive analysis of uncertainties indicates a 49.14% level of uncertainty in the forest AGB estimation and we found that most uncertainties can be attributed to errors in allometric models and in height measurements by spaceborne LiDAR.

Our study illustrates the value of using spaceborne LiDAR data by extending limited field biomass plots to a bigger set of GLAS spots. Our study also assesses the importance of multi-seasonal Landsat data and PALSAR data for large-scale forest AGB estimation. Our forest AGB map can serve as a baseline map for studying forest carbon stocks and

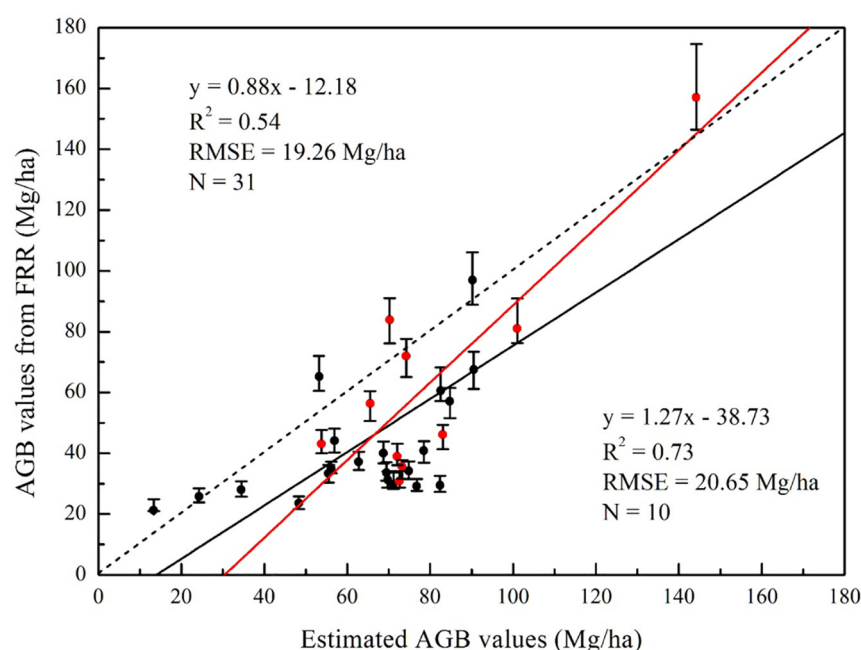


Fig. 10. Comparison of the estimated AGB and AGB from the Chinese forest resource reports (FRR). The error bar denotes the range of forest AGB for each province, the gray line and red line are regression curves for all thirty-one provinces in mainland China ($R^2 = 0.54$, $RMSE = 19.26$ Mg/ha, $N = 31$) and top ten provinces in forested area ($R^2 = 0.73$, $RMSE = 20.65$ Mg/ha, $N = 10$), respectively, the dotted line is 1:1 line. (For interpretation of the references to color in this figure legend, the reader is referred to the web version of this article.)

Table 2
Comparisons of national average forest AGB derived from various studies.

| Source | Average AGB (Mg/ha) | Resolution (m) | Time interval |
|---------------|---------------------|----------------|---------------|
| In this study | 69.88 | 30 | 2006 |
| Piao et al. | 73.4 | 8000 | 1981–1999 |
| Yu et al. | 64.2 | | 1980s–2003 |
| Du et al. | 61.8 | ~5600 | 2004–2008 |
| Su et al. | 120 | 1000 | 2004 |
| Yin et al. | 112.2 | 1000 | 2001–2013 |

related changes across China. Future work should focus on monitoring biomass carbon changes based on forest area dynamics and estimating biomass using new spaceborne LiDAR, high resolution optical and SAR data.

Acknowledgments

This study was supported by the Strategic Priority Research Program of Chinese Academy of Sciences (XDA19070202), the National Key R&D Program of China (2017YFA0604401 and 2018YFC1407103), and the Special Fund for Meteorology Scientific Research in the Public Welfare (GYHY201506010). This study also largely benefited from the language revision by Pauline Lovell and Arthur Cracknell and helpful suggestions of the three reviewers. Our AGB data is available from the corresponding author upon request.

Appendix A. Supplementary data

Supplementary data to this article can be found online at <https://doi.org/10.1016/j.rse.2018.11.017>.

References

- Asner, G.P., Hughes, R.F., Mascaro, J., Uowolo, A.L., Knapp, D.E., Jacobson, J., Kennedy-Bowdoin, T., Clark, J.K., 2011. High-resolution carbon mapping on the million-hectare Island of Hawaii. *Front. Ecol. Environ.* 9, 434–439.
- Baghdadi, N., Maire, G.L., Bailly, J.S., Osé, K., Nouvellon, Y., Zribi, M., Lemos, C., Hakamada, R., 2015. Evaluation of ALOS/PALSAR L-band data for the estimation of eucalyptus plantations aboveground biomass in Brazil. *IEEE J. Sel. Top. Appl. Earth Obs. Remote Sens.* 8, 3802–3811.
- Belgiu, M., Drăguț, L., 2016. Random forest in remote sensing: a review of applications and future directions. *ISPRS J. Photogramm. Remote Sens.* 114, 24–31.

- Boisvenue, C., Smiley, B.P., White, J.C., Kurz, W.A., Wulder, M.A., 2016. Integration of Landsat time series and field plots for forest productivity estimates in decision support models. *For. Ecol. Manag.* 376, 284–297.
- Cao, L., Coops, N.C., Innes, J.L., Sheppard, S.R.J., Fu, L., Ruan, H., She, G., 2016. Estimation of forest biomass dynamics in subtropical forests using multi-temporal airborne LiDAR data. *Remote Sens. Environ.* 178, 158–171.
- Cartus, O., Kelldorfer, J., Walker, W., Franco, C., Bishop, J., Santos, L., Fuentes, J., 2014. A national, detailed map of forest aboveground carbon stocks in Mexico. *Remote Sens.* 6, 5559.
- Castel, T., Beaudoin, A., Picard, G., Thuy Le, T., Caraglio, Y., Houllier, F., 2000. An accurate analysis of L-band SAR backscatter sensitivity to forest biomass. In: *IEEE 2000 International Geoscience and Remote Sensing Symposium. Taking the Pulse of the Planet: The Role of Remote Sensing in Managing the Environment*. 6. pp. 2564–2566.
- Chave, J., Condit, R., Aguilar, S., Hernandez, A., Lao, S., Perez, R., 2004. Error propagation and scaling for tropical forest biomass estimates. *Philos. Trans. R. Soc. Lond. Ser. B Biol. Sci.* 359, 409–420.
- Chen, Q., Vaglio Laurin, G., Valentini, R., 2015. Uncertainty of remotely sensed aboveground biomass over an African tropical forest: propagating errors from trees to plots to pixels. *Remote Sens. Environ.* 160, 134–143.
- Chen, Q., McRoberts, R.E., Wang, C., Radtke, P.J., 2016. Forest aboveground biomass mapping and estimation across multiple spatial scales using model-based inference. *Remote Sens. Environ.* 184, 350–360.
- Cheng, D.-L., Wang, G.-X., Li, T., Tang, Q.-L., Gong, C.-M., 2007. Relationships among the stem, aboveground and total biomass across Chinese forests. *J. Integr. Plant Biol.* 49, 1573–1579.
- Chi, H., Sun, G., Huang, J., Guo, Z., Ni, W., Fu, A., 2015. National forest aboveground biomass mapping from ICESat/GLAS data and MODIS imagery in China. *Remote Sens.* 7, 5534.
- CMF (Chinese Ministry of Forestry), 2014. *Forest Resource Report of China for Periods 2009–2013*. Department of Forest Resource and Management. Chinese Ministry of Forestry, Beijing.
- Connors, R.W., Trivedi, M.M., Harlow, C.A., 1984. Segmentation of a high-resolution urban scene using texture operators. *Comput. Vis. Graph. Image Process.* 25, 273–310.
- Dobson, M.C., Ulabay, F.T., Letoan, T., Beaudoin, A., Kasischke, E.S., Christensen, N., 1992. Dependence of radar backscatter on coniferous forest biomass. *IEEE Trans. Geosci. Remote Sens.* 30, 412–415.
- Dong, J., Ma, Y., Sun, H., 2016. From pilot to the National Emissions Trading Scheme in China: international practice and domestic experiences. *Sustainability* 8, 522.
- Du, L., Zhou, T., Zou, Z., Zhao, X., Huang, K., Wu, H., 2014. Mapping forest biomass using remote sensing and National Forest Inventory in China. *Forests* 5, 1267.
- Duncanson, L., Rourke, O., Dubayah, R., 2015. Small sample sizes yield biased allometric equations in temperate forests. *Sci. Rep.* 5, 17153.
- Fang, J.-Y., Wang, G.G., Liu, G.-H., Xu, S.-L., 1998. Forest biomass of China: an estimate based on the biomass-volume relationship. *Ecol. Appl.* 8, 1084–1091.
- Ferrazzoli, P., Guerriero, L., 1995. Radar sensitivity to tree geometry and woody volume: a model analysis. *IEEE Trans. Geosci. Remote Sens.* 33, 360–371.
- Food, G.M., Boyd, D.S., Cutler, M.E.J., 2003. Predictive relations of tropical forest biomass from Landsat TM data and their transferability between regions. *Remote Sens. Environ.* 85, 463–474.
- Fu, B.-J., Liu, G.-H., Lü, Y.-H., Chen, L.-D., Ma, K.-M., 2004. Ecoregions and ecosystem management in China. *Int J. Sust. Dev. World* 11, 397–409.

- Gong, P., 2012. Remote sensing of environmental change over China: a review. *Chin. Sci. Bull.* 57, 2793–2801.
- Gong, P., Sheng, Y., Bliging, G.S., 2002. 3D model-based tree measurement from high resolution aerial imagery. *Photogramm. Eng. Remote. Sens.* 68, 1203–1212.
- Gong, P., Li, Z., Huang, H., Sun, G., Wang, L., 2011. ICESat GLAS data for urban environment monitoring. *IEEE Trans. Geosci. Remote Sens.* 49, 1158–1172.
- Hall, F.G., Bergen, K., Blair, J.B., Dubayah, R., Houghton, R., Hurr, G., Kellendorfer, J., Lefsky, M., Ranson, J., Saatchi, S., Shugart, H.H., Wickland, D., 2011. Characterizing 3D vegetation structure from space: mission requirements. *Remote Sens. Environ.* 115, 2753–2775.
- Hansen, M.C., Potapov, P.V., Goetz, S.J., Turubanova, S., Tyukavina, A., Krylov, A., Kommareddy, A., Egorov, A., 2016. Mapping tree height distributions in sub-Saharan Africa using Landsat 7 and 8 data. *Remote Sens. Environ.* 185, 221–232.
- Haralick, R.M., Shanmugam, K., Dinstein, I., 1973. Textural features for image classification. *IEEE Trans. Syst. Man Cybern. SMC-3*, 610–621.
- Huang, H., Gong, P., Cheng, X., Clinton, N., Li, Z., 2009. Improving measurement of forest structural parameters by co-registering of high resolution aerial imagery and low density LiDAR data. *Sensors* 9, 1541–1558.
- Huang, H., Liu, C., Wang, X., Biging, G.S., Chen, Y., Yang, J., Gong, P., 2017. Mapping vegetation heights in China using slope correction ICESat data, SRTM, MODIS-derived and climate data. *ISPRS J. Photogramm. Remote Sens.* 129, 189–199.
- Huang, H., Liu, C., Wang, X., Gong, P., 2018. Constructing a finer-resolution forest height map of China using ICESat/GLAS, Landsat and ALOS PALSAR data and height patterns of natural forests and plantations. *Agric. For. Meteorol.* (under review).
- Jucker, T., Caspersen, J., Chave, J., Antin, C., Barbier, N., Bongers, F., Dalponte, M., van Ewijk, K.Y., Forrester, D.L., Haeni, M., Higgins, S.L., Holdaway, R.J., Iida, Y., Lorimer, C., Marshall, P.L., Momo, S., Moncrieff, G.R., Ploton, P., Poorter, L., Rahman, K.A., Schlund, M., Sonké, B., Sterck, F.J., Trugman, A.T., Usoltsev, V.A., Vanderwel, M.C., Waldner, P., Wedeux, B.M.M., Wirth, C., Wöll, H., Woods, M., Xiang, W., Zimmermann, N.E., Coomes, D.A., 2017. Allometric equations for integrating remote sensing imagery into forest monitoring programmes. *Glob. Chang. Biol.* 23, 177–190.
- Le Toan, T., Quegan, S., Davidson, M.W.J., Balzter, H., Paillou, P., Papathanassiou, K., Plummer, S., Rocca, F., Saatchi, S., Shugart, H., Ulander, L., 2011. The BIOMASS mission: mapping global forest biomass to better understand the terrestrial carbon cycle. *Remote Sens. Environ.* 115, 2850–2860.
- Lefsky, M.A., Harding, D., Cohen, W.B., Parker, G.G., Shugart, H.H., 1999. Surface Lidar remote sensing of basal area and biomass in deciduous forests of eastern Maryland, USA. *Remote Sens. Environ.* 67, 83–98.
- Lefsky, M.A., Keller, M., Pang, Y., Camargo, P.B.d., Hunter, M.O., 2007. Revised method for forest canopy height estimation from Geoscience Laser Altimeter System waveforms. *J. Appl. Remote. Sens.* 1, 013537.
- Li, C., Wang, J., Hu, L., Yu, L., Clinton, N., Huang, H., Yang, J., Gong, P., 2014. A circa 2010 thirty meter resolution forest map for China. *Remote Sens.* 6, 5325–5343.
- Liu, C., Huang, H., Gong, P., Wang, X., Wang, J., Li, W., Li, C., Li, Z., 2015. Joint use of ICESat/GLAS and Landsat data in land cover classification: a case study in Henan Province, China. *IEEE J. Sel. Top. Appl. Earth Obs. Remote Sens.* 8, 511–522.
- Liu, C., Zhou, X., Lei, X., Huang, H., Peng, C., Wang, X., Sun, J., Zhou, C., 2017. Reducing the Uncertainty in the Forest Volume-to-biomass Relationship Built From Limited Field Plots. *ArXiv e-prints*. pp. 1702.
- Luo, Y., Wang, X., Zhang, X., Lu, F., 2013. Biomass and its Allocation of Forest Ecosystems in China. Chinese Forestry Publishing House Press, Beijing.
- Moore, I.D., Grayson, R.B., Ladson, A.R., 1991. Digital terrain modelling: a review of hydrological, geomorphological, and biological applications. *Hydrol. Process.* 5, 3–30.
- Nelson, R., Margolis, H., Montesano, P., Sun, G., Cook, B., Corp, L., Andersen, H.-E., deJong, B., Pellat, F.P., Fickel, T., Kauffman, J., Pringle, S., 2017. Lidar-based estimates of aboveground biomass in the continental US and Mexico using ground, airborne, and satellite observations. *Remote Sens. Environ.* 188, 127–140.
- Pettorelli, N., Wegmann, M., Skidmore, A., Muecher, S., Dawson, T.P., Fernandez, M., Lucas, R., Schaepman, M.E., Wang, T., O'Connor, B., Jongman, R.H.G., Kempeneers, P., Sonnenschein, R., Leidner, A.K., Böhm, M., He, K.S., Nagendra, H., Dubois, G., Fatoyinbo, T., Hansen, M.C., Paganini, M., de Klerk, H.M., Asner, G.P., Kerr, J.T., Estes, A.B., Schmeller, D.S., Heiden, U., Rocchini, D., Pereira, H.M., Turak, E., Fernandez, N., Lausch, A., Cho, M.A., Alcaraz-Segura, D., McGeoch, M.A., Turner, W., Mueller, A., St-Louis, V., Penner, J., Vihervaara, P., Belward, A., Meyers, B., Geller, G.N., 2016. Framing the concept of satellite remote sensing essential biodiversity variables: challenges and future directions. *Remote Sens. Ecol. Conserv.* 2, 122–131.
- Pflugmacher, D., Cohen, W.B., Kennedy, R.E., Yang, Z., 2014. Using Landsat-derived disturbance and recovery history and lidar to map forest biomass dynamics. *Remote Sens. Environ.* 151, 124–137.
- Piao, S., Fang, J., Zhu, B., Tan, K., 2005. Forest biomass carbon stocks in China over the past 2 decades: estimation based on integrated inventory and satellite data. *J. Geophys. Res. Biogeosci.* 110, G01006.
- Qin, Y., Xiao, X., Dong, J., Zhang, G., Shimada, M., Liu, J., Li, C., Kou, W., Moore, Iii, B., 2015. Forest cover maps of China in 2010 from multiple approaches and data sources: PALSAR, Landsat, MODIS, FRA, and NFI. *ISPRS J. Photogramm. Remote Sens.* 109, 1–16.
- Reuter, H.I., Nelson, A., Jarvis, A., 2007. An evaluation of void-filling interpolation methods for SRTM data. *Int. J. Geogr. Inf. Sci.* 21, 983–1008.
- Rignot, E., 1996. Dual-frequency interferometric SAR observations of a tropical rainforest. *Geophys. Res. Lett.* 23, 993–996.
- Rodríguez-Veiga, P., Saatchi, S., Tansey, K., Balzter, H., 2016. Magnitude, spatial distribution and uncertainty of forest biomass stocks in Mexico. *Remote Sens. Environ.* 183, 265–281.
- Saatchi, S.S., Harris, N.L., Brown, S., Lefsky, M., Mitchard, E.T.A., Salas, W., Zutta, B.R., Buermann, W., Lewis, S.L., Hagen, S., Petrova, S., White, L., Silman, M., Morel, A., 2011. Benchmark map of forest carbon stocks in tropical regions across three continents. *Proc. Natl. Acad. Sci.* 108, 9899–9904.
- Santi, E., Paloscia, S., Pettinato, S., Fontanelli, G., Mura, M., Zolli, C., Maselli, F., Chiesi, M., Bottai, L., Chirici, G., 2017. The potential of multifrequency SAR images for estimating forest biomass in Mediterranean areas. *Remote Sens. Environ.* 200, 63–73.
- Sarker, M.L.R., Nichol, J., Iz, H.B., Ahmad, B.B., Rahman, A.A., 2013. Forest biomass estimation using texture measurements of high-resolution dual-polarization C-band SAR data. *IEEE Trans. Geosci. Remote Sens.* 51, 3371–3384.
- Sexton, J.O., Song, X.-P., Feng, M., Noojipady, P., Anand, A., Huang, C., Kim, D.-H., Collins, K.M., Channan, S., DiMiceli, C., Townshend, J.R., 2013. Global, 30-m resolution continuous fields of tree cover: Landsat-based rescaling of MODIS vegetation continuous fields with lidar-based estimates of error. *Int. J. Digital Earth* 6, 427–448.
- Shimada, M., Itoh, T., Motooka, T., Watanabe, M., Shiraishi, T., Thapa, R., Lucas, R., 2014. New global forest/non-forest maps from ALOS PALSAR data (2007–2010). *Remote Sens. Environ.* 155, 13–31.
- Simard, M., Pinto, N., Fisher, J.B., Baccini, A., 2011. Mapping forest canopy height globally with spaceborne lidar. *J. Geophys. Res. Biogeosci.* 116, G04021.
- Su, Y., Guo, Q., Xue, B., Hu, T., Alvarez, O., Tao, S., Fang, J., 2016. Spatial distribution of forest aboveground biomass in China: estimation through combination of spaceborne lidar, optical imagery, and forest inventory data. *Remote Sens. Environ.* 173, 187–199.
- Sun, G., Ranson, K.J., Guo, Z., Zhang, Z., Montesano, P., Kimes, D., 2011. Forest biomass mapping from lidar and radar synergies. *Remote Sens. Environ.* 115, 2906–2916.
- Thapa, R.B., Watanabe, M., Motooka, T., Shimada, M., 2015. Potential of high-resolution ALOS-PALSAR mosaic texture for aboveground forest carbon tracking in tropical region. *Remote Sens. Environ.* 160, 122–133.
- Thiel, C., Schmullius, C., 2016. The potential of ALOS PALSAR backscatter and InSAR coherence for forest growing stock volume estimation in Central Siberia. *Remote Sens. Environ.* 173, 258–273.
- Ulab, F.T., Whitt, M.W., Dobson, M.C., 1990. Measuring the propagation properties of a forest canopy using a polarimetric scatterometer. *IEEE Trans. Antennas Propag.* 38, 251–258.
- Villard, L., Le Toan, T., Ho Tong Minh, D., Mermoz, S., Bouvet, A., 2016. Forest biomass from radar remote sensing. In: Zribi, M. (Ed.), *Land Surface Remote Sensing in Agriculture and Forest*. Elsevier, pp. 363–425.
- Wang, X., Huang, H., Gong, P., Liu, C., Li, C., Li, W., 2014. Forest canopy height extraction in rugged areas with ICESat/GLAS data. *IEEE Geosci. Remote Sens. Lett.* 52, 4650–4657.
- Yin, G., Zhang, Y., Sun, Y., Wang, T., Zeng, Z., Piao, S., 2015. MODIS based estimation of Forest aboveground biomass in China. *PLoS One* 10, e0130143.
- Yu, G., Li, X., Wang, Q., Li, S., 2010. Carbon storage and its spatial pattern of terrestrial ecosystem in China. *J. Resour. Ecol.* 1, 97–109.
- Zanne, A., Lopez-Gonzalez, G., Coomes, D., Ilc, J., Jansen, S., Lewis, S., Miller, R., Swenson, N., Wiemann, M., Chave, J., 2009. Data from: towards a worldwide wood economics spectrum. *Dryad Digit. Repository*. <https://doi.org/10.5061/dryad.234>.
- Zeng, W., Tomppo, E., Healey, S., Gadov, K., 2015. The national forest inventory in China: history - results - international context. *For. Ecosyst.* 2, 23.
- Zhou, X., Lei, X., Peng, C., Wang, W., Zhou, C., Liu, C., Liu, Z., 2016. Correcting the overestimate of forest biomass carbon on the national scale. *Methods Ecol. Evol.* 7, 447–455.
- Zhu, Z., Wang, S., Woodcock, C.E., 2015. Improvement and expansion of the Fmask algorithm: cloud, cloud shadow, and snow detection for Landsats 4–7, 8, and Sentinel 2 images. *Remote Sens. Environ.* 159, 269–277.
- Zhu, J., Hu, H., Tao, S., Chi, X., Li, P., Jiang, L., Ji, C., Zhu, J., Tang, Z., Pan, Y., Birdsey, R.A., He, X., Fang, J., 2017. Carbon stocks and changes of dead organic matter in China's forests. *Nat. Commun.* 8, 151.
- Zwally, H.J., Schutz, R., Bentley, C., Bufton, J., Herring, T., Minster, J., Spinhrine, J., Thomas, R., 2011. GLAS/ICESat L1A Global Altimetry Data, Version 33. NASA National Snow and Ice Data Center Distributed Active Archive Center, Boulder, Colorado USA.